

# **MIDAR: Mimicking LiDAR Detection for Traffic Applications with a Lightweight Plug-and-Play Model**

**Tianheng Zhu**

Lyles School of Civil and Construction Engineering

Purdue University

550 Stadium Mall Drive, West Lafayette, IN, United States, 47907

Email: [zhu1230@purdue.edu](mailto:zhu1230@purdue.edu)

**Yiheng Feng\***

Lyles School of Civil and Construction Engineering

Purdue University

550 Stadium Mall Drive, West Lafayette, IN, United States, 47907

Email: [feng333@purdue.edu](mailto:feng333@purdue.edu)

\*Corresponding author

## **ABSTRACT**

As autonomous driving (AD) technology advances, increasing research has focused on leveraging cooperative perception (CP) data collected from multiple AVs to enhance traffic applications. Due to the impracticality of large-scale real-world AV deployments, simulation has become the primary approach in most studies. While game-engine-based simulators like CARLA generate high-fidelity raw sensor data (e.g., LiDAR point clouds) which can be used to produce realistic detection outputs, they face scalability challenges in multi-AV scenarios. In contrast, microscopic traffic simulators such as SUMO scale efficiently but lack perception modeling capabilities. To bridge this gap, we propose MIDAR, a LiDAR detection mimicking model that approximates realistic LiDAR detections using vehicle-level features readily available from microscopic traffic simulators. Specifically, MIDAR predicts true positives (TPs) and false negatives (FNs) from ideal LiDAR detection results based on the spatial layouts and dimensions of surrounding vehicles. A Refined Multi-hop Line-of-Sight (RM-LoS) graph is constructed to encode the occlusion relationships among vehicles, upon which MIDAR employs a GRU-enhanced APPNP architecture to propagate features from the ego AV and occluding vehicles to the prediction target. MIDAR achieves an AUC of 0.909 in approximating the detection results generated by CenterPoint, a mainstream 3D LiDAR detection model, on the nuScenes AD dataset. Two CP-based traffic applications further validate the necessity of such realistic detection modeling, particularly for tasks requiring accurate individual vehicle observations (e.g., position, speed, lane index). As demonstrated in the applications, MIDAR can be seamlessly integrated into traffic simulators and trajectory datasets and will be open-sourced upon publication.

**Keywords:** Cooperative perception, LiDAR detection modeling, line-of-sight graph, graph neural network, microscopic traffic simulation, vehicle trajectory dataset

## 1. INTRODUCTION

Waymo’s recent achievement of accumulating over 100 million driverless miles has marked a significant milestone for autonomous vehicles (AV) (1), indicating great potentials for large-scale real-world deployment in the near future. Numerous studies have been conducted to evaluate the impact of AVs, especially in a mixed traffic condition, on transportation system safety (2; 3), mobility (4-6), sustainability (7), and cybersecurity (8). The vast majority of these studies are conducted in a simulation environment because such large-scale real-world testing like Waymo is not realistic for most researchers due to high financial investment, extensive technical preparation, and potential public safety risks.

To mimic AV systems in simulation, generating sensor data is a fundamental requirement. Game-engine-based simulation platforms (i.e., high-fidelity simulators), such as CARLA (9), LGSVL (10), and AirSim (11), support flexible setup of multi-modality sensor suites and provide raw sensor signals, like RGB camera images and LiDAR point clouds. Computer vision algorithms can be directly applied to these simulated sensor outputs to generate detection results. These high-fidelity simulators are usually served as the closed-loop benchmarking platforms to test and validate Autonomous Driving (AD) algorithms and strategies, including sensor perception, vehicle localization, traffic prediction, path planning, and vehicle control. Expanding to multiple AVs, the idea of cooperative perception (CP) was proposed to address the inevitable physical occlusion and limited receptive field of single vehicles (12), by sharing and fusing the sensor information from multiple perception nodes (PNs). Recent studies show benefits of CP in many traffic applications including cooperative driving (13), traffic signal control (14), and trajectory reconstruction (15). However, testing and evaluating CP-based applications using high-fidelity simulators are highly resource-intensive, due to the computational demands of generating signals for multiple AVs and PNs in real time. Especially for network-level applications such as CAV-based routing (16; 17), there may exist dozens if not hundreds of CAVs in the network at the same time, making real-time generation of sensor data and rendering the physical environment impossible, even with high-end computation platforms.

As an alternative approach, microscopic traffic simulation platforms, like SUMO and VISSIM, are widely employed to develop and evaluate CP-based applications. Since traffic simulators only provide vehicle-level information and do not natively support raw sensor data generation and/or perception modeling for simulated AVs, simplified or aggregated models are used to mimic the detection results of real perception sensors. For example, Li et al. (18) assumed perfect detection (i.e., all vehicle can be detected accurately) within the sensor range of AVs to estimate and predict the microscopic vehicle states. To take a step forward, Li et al. (14) incorporated the aggregated precision results of a LiDAR detection algorithm into SUMO. Specifically, vehicles within the AV detection range are randomly dropped (i.e., considered to be unobserved) based on a probability that decreases with the increase of distance. In addition to traffic simulation platforms, many studies that do not require interactive environments were conducted on vehicle trajectory datasets and utilized post-processing steps to mimic data generated from AV perception sensors. For instance, Zhang and Feng (15) developed a trajectory reconstruction model that utilizes partial observations of AVs to recover complete vehicle trajectories on freeways. To approximate AV detection results, they modelled occlusions within AV detection range based on vehicle size and location via a rule-based approach. However, detection results from all these simplified models still differ significantly from the actual detection pipeline that applies object detection algorithms to raw sensor signals.

In summary, while high-fidelity simulators can generate realistic detection results for AVs as in real-world deployment, they face scalability challenges when applied to scenarios involving large network and multiple AVs. On the other hand, microscopic traffic simulators can efficiently simulate large numbers of AVs, but struggle to approximate realistic detection outputs. To reconcile the trade-off between scalability and detection realism, we develop MIDAR, a light-weight Graph Neural Network (GNN) model that mimics LiDAR detection results based on the spatial configuration (i.e., layout) and vehicle-level features of surrounding vehicles relative to the sensor. A Refined Multi-hop Line-of-Sight (RM-LoS) graph is proposed to help MIDAR capture the impact of the aforementioned surrounding vehicles’ layout and features on detection errors. The model can be seamlessly integrated into microscopic traffic simulators like SUMO or directly applied to existing vehicle trajectory datasets to produce LiDAR detection results that are close to reality. The MIDAR model is trained and evaluated using nuScenes AD dataset (19) and

the CenterPoint (20) LiDAR detection algorithm. Furthermore, to demonstrate the necessity of modeling realistic detection results, we conduct case studies on two CP-based traffic applications (i.e., CP-based traffic signal control and vehicle trajectory reconstruction). Results show that different detection models result in significant differences in the application’s performance metrics (e.g., average vehicle delay at intersections, and mean average error (MAE) in reconstructed trajectories).

Our major contributions are outlined below:

- (1) The proposed MIDAR model is one of the first works that try to close the gap between simulation scalability and detection realism for CP-based research. The model inference is highly efficient and can be easily incorporated to microscopic traffic simulators and vehicle trajectory datasets.
- (2) Validated by a popular AD dataset (nuScenes) and a mainstream LiDAR detection model (CenterPoint), MIDAR shows high accuracy in approximating realistic LiDAR detection results.
- (3) Experiments with two CP-based traffic applications validate the necessity of such modeling, by showing simplified detection models may generate overestimated performance metrics.
- (4) Although designed for LiDAR detection, the MIDAR framework can also be applied to other sensing modalities such as camera or multi-sensor fusion.

## 2. METHODOLOGY

We begin by presenting the problem statement. Then, detailed methodologies, including construction of the graphs and the GNN architecture, are introduced.

### 2.1 Problem Statement

The proposed MIDAR model aims to approximate the detection results of a single LiDAR sensor. Sensor fusion from multiple LiDARs and/or from other modalities (e.g., camera) are not considered in the scope of this paper. However, the proposed mimicking framework can be potentially applied to other types of sensors. The implementation of the MIDAR model requires complete information on all vehicle states in the detection range of the ego vehicle (i.e., AV). As a result, MIDAR can be implemented in microscopic traffic simulator or trajectory datasets with ground-truth data (NGSIM, HighD, etc.). Note that in these trajectory datasets, vehicle height may not be available and needs to be approximated based on vehicle length and width.

The LiDAR detection results can be categorized as True Positives (TPs), False Negatives (FNs) and False Positives (FPs). A TP indicates a correctly detected object. An FN occurs when the detector fails to identify an object that’s actually present in the scene, while an FP refers to detection of a non-existent object. In this paper, MIDAR focuses solely on modeling TP and errors from FNs. FNs represent the primary source of detection errors and can be approximated without the raw point cloud data, as opposed to FP. The major reasons for FNs include occlusion and distance, as the sensor cannot “see” through opaque objects or too far away from the object, leading to unobserved regions or limited laser points projected onto objects (21). Therefore, the spatial layouts and vehicle-level features (e.g., locations, dimensions, headings, distance to the ego AV) of surrounding vehicles can be used to predict FNs. Modeling FP errors is more difficult and will be investigated in the future research.

**Figure 1** illustrates the workflow of MIDAR. Starting from the bird’s-eye view (BEV) of a traffic scene, a RM-LoS graph is first constructed, where each node represents a vehicle and is encoded with features including vehicle position ( $x, y, z$ ), dimensions ( $w, l, h$ ), heading, and direct distance to the AV. These features are first converted into node embeddings via a Multi-Layer Perceptron (MLP), then propagated using the approximate personalized PageRank algorithm. The resulting representations are refined through a Gated Recurrent Unit (GRU), followed by a linear decoder that predicts whether a real vehicle is detected or not. In this way, MIDAR approximates realistic LiDAR detection results in terms of TPs and FNs, as shown in Figure 1.d.

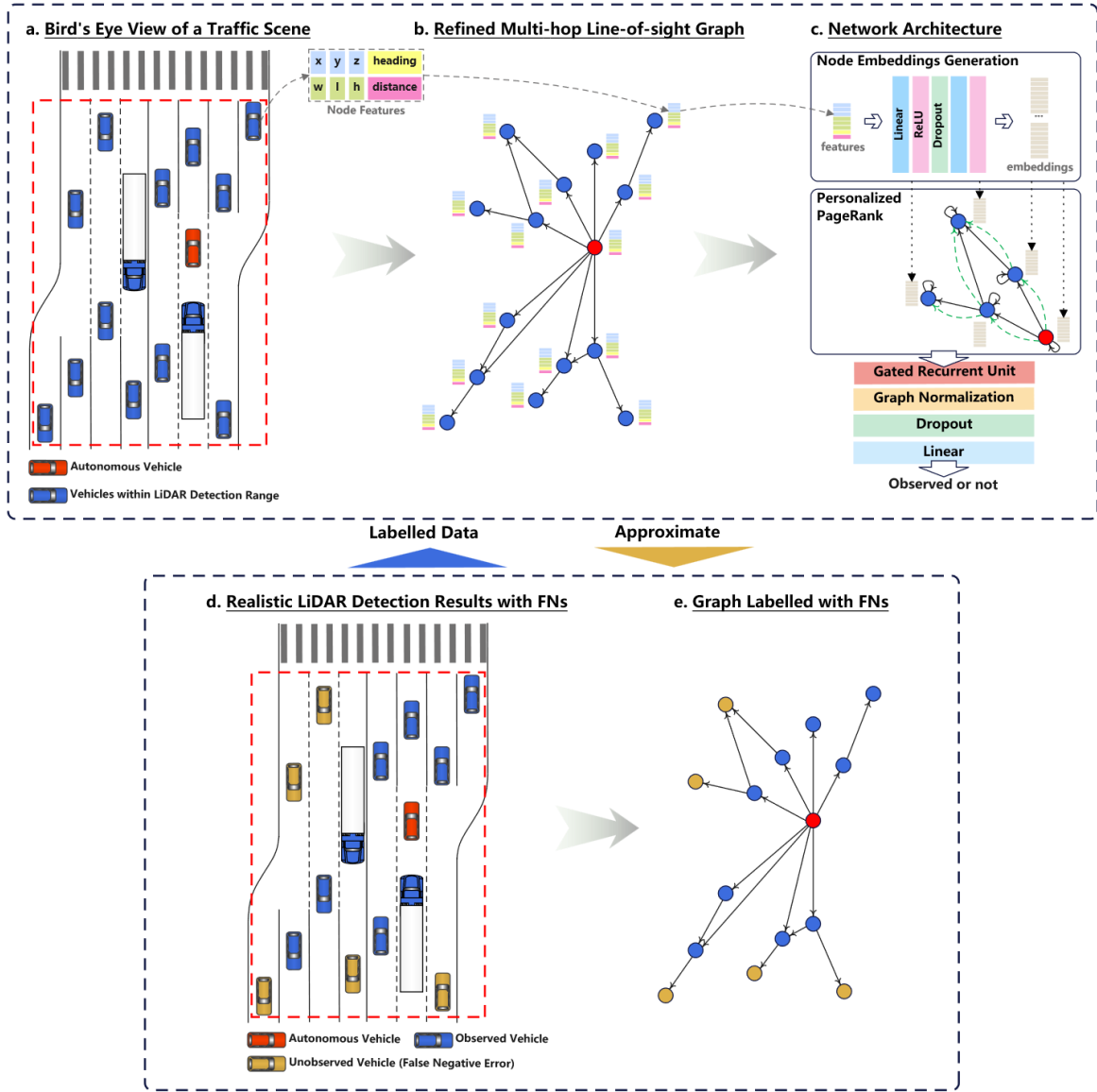


Figure 1 Illustration of MIDAR Workflow

## 2.2 Construction of RM-LoS Graphs

A RM-LoS graph is constructed to better capture the influence of the layout and features of surrounding vehicles on FN detection errors.

The concept of Line-of-Sight (LoS) graph was firstly introduced by (22) for testing printed circuit boards for potential short circuits. The perception of AVs can be represented using LoS graphs, with surrounding vehicles connected only if there is a direct, unobstructed line of sight from the ego AV. For example, given the traffic scene in **Figure 2.a**, the constructed LoS graph is illustrated in **Figure 2.b.1**.

However, this basic LoS representation may not fully capture the complexities of LiDAR perception, as partial occlusions (or equivalently partial observation) can still generate detectable features. Therefore, the LoS graph is extended to a multi-hop LoS graph, in which surrounding vehicles are considered to be connected to the ego AV via intermediate nodes, as shown in **Figure 2.b.2**. For example, even if the LiDAR cannot directly observe vehicle “h” without obstruction, it may still be connected to “h” through vehicle “g”, as long as both LoS connections exist. However, the multi-hop LoS graph can introduce excessive non-informative edges, complicating message passing. As illustrated in **Figure 2.b.2**,

it is unlikely that vehicle “j” has any meaningful influence on vehicle “b” in the context of detection errors. Meanwhile, bidirectional edges do not reflect the unidirectional nature of AV perception, where the AV gathers information from surrounding vehicles, but not vice versa.

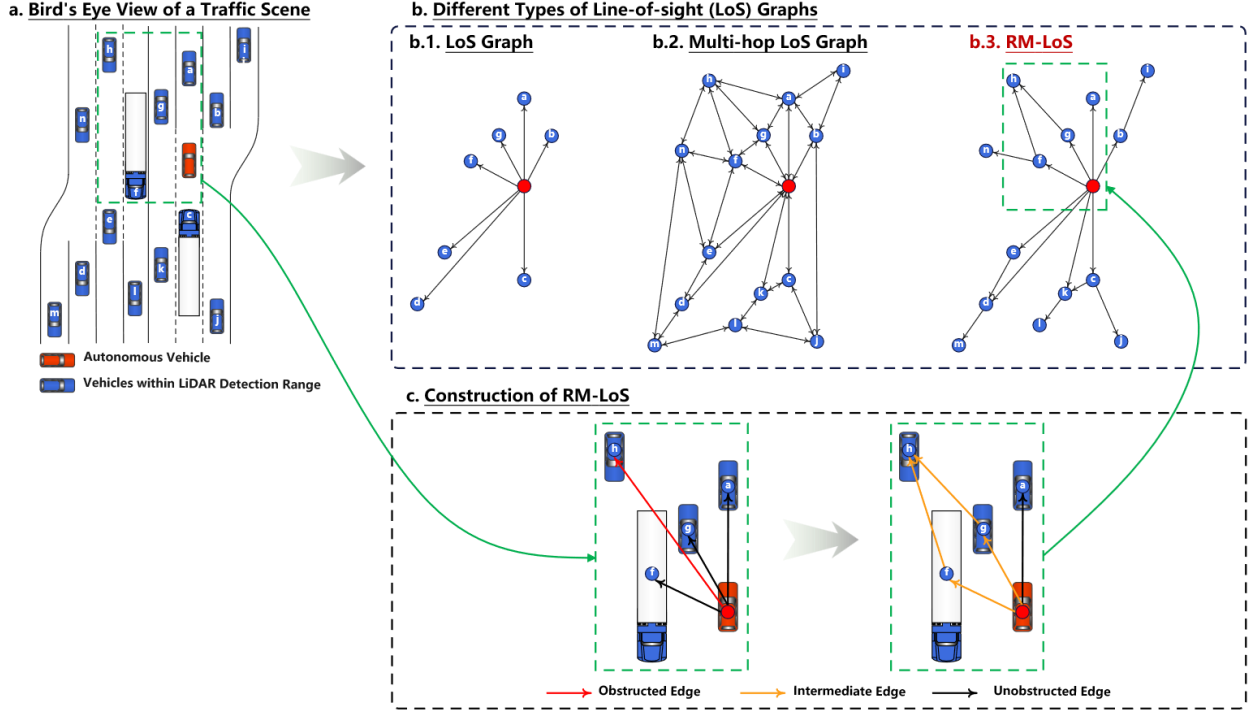


**Figure 2 Comparison between different types of LoS graphs**

To address the above limitations, we present RM-LoS, a refined multi-hop LoS graph. Using the same traffic scene in **Figure 2.a** as an illustration, the RM-LoS is constructed with the following three steps:

- (1) Select one surrounding vehicle within LiDAR detection range, connect an edge from the center of the AV to the center of the selected vehicle.
- (2) If this edge intersects with any other vehicles (i.e., the edge is obstructed), it is segmented into multiple intermediate edges. Specifically, the intermediate edges first originate from the AV to the intersecting vehicles, then from the intersecting vehicles to the target vehicle.
- (3) Repeat Steps 1 and 2 for all vehicles.

It’s worth noting that 1) the vehicle selection sequence can be arbitrary; and 2) all the constructed edges in RM-LoS are unidirectional, originating from the AV to surrounding vehicles, or from nearer to farther vehicles, to better reflect the occlusion relationship between vehicles.

**Figure 2.c** shows an example for the construction of RM-LoS among truck “f”, vehicle “g”, vehicle “h”, and the AV, the edge connecting vehicle “h” and the AV would intersect with truck “f” and vehicle “g”. Therefore, it’s segmented into 4 intermediate edges (AV to “f”, AV to “g”, “f” to “h”, “g” to “h”), meaning that the detection of vehicle “h” is associated to the features (e.g., locations and sizes) of truck “f” and vehicle “g”.

As illustrated in **Figure 1**, the edges in a RM-LoS graph serve solely as message-passing pathways without edge attributes. Each node represents a vehicle and encodes vehicle-level features, including vehicles’ 3D position in the Cartesian coordinates of the LiDAR sensor frame (i.e.,  $x, y, z$ ), physical dimensions (i.e., width, length, height), heading, and direct distance from the ego AV. Based on the constructed RM-LoS graph and defined node features, a graph neural network is constructed in the next section.

### 2.3 Network Architecture

The architecture of MIDAR follows the Approximated Personalized PageRank of Neural Predictions (APPNP) (23), a simple yet effective model for node classification tasks on graphs. After generating the embeddings for each node in the graph using a MLP, the node embeddings are propagated using an adaptation of personalized PageRank.

The final node representations of APPNP,  $Z^{(K)}$ , are obtained through  $K$  power iterations, where each iteration propagates information across the graph while blending in the original embeddings, as defined from **Equation (2.1)** to **(2.3)**. The number of iterations,  $K$ , determines the maximum information propagation range (i.e., how many hops away a node can receive information from), while the teleport probability,  $\alpha$ , governs how much of the original embedding is retained at each step to mitigate over-smoothing.

$$Z^{(0)} = H = f_{\theta}(X) \quad (2.1)$$

$$Z^{(k+1)} = (1 - \alpha)\hat{A}Z^{(k)} + \alpha H \quad (2.2)$$

$$Z^{(K)} = \text{softmax}\left((1 - \alpha)\hat{A}Z^{(K-1)} + \alpha H\right) \quad (2.3)$$

where  $X$  is the feature matrix.  $f_{\theta}$  is the MLP with parameter set  $\theta$  generating the original node embeddings  $H$ . As mentioned above,  $K$  is the number of power iterations,  $k \in [0, K - 2]$  is the iteration step.  $Z^{(k)}$  is the node representation at the  $k^{\text{th}}$  iteration.  $\hat{A}$  is a propagation matrix (e.g., adjacency matrix).  $\alpha \in (0, 1]$  is the teleport probability. The final *softmax* function produces a class probability distribution for each node.

APPNP approximates the matrix inverse in Personalized PageRank of Neural Predictions (PPNP)'s model equations (defined in **Equation (2.4)**) via power iterations and achieves linear computational complexity, which makes it a computationally efficient alternative to PPNP.

$$Z_{PPNP} = \text{softmax}\left(\alpha(I_n - (1 - \alpha)\hat{A})^{-1}H\right) \quad (2.4)$$

where  $I_n$  is a  $n$  by  $n$  identity matrix.

Compared to other GNNs designed for node classification, such as Graph Convolutional Networks (GCNs), APPNP enables deeper information propagation without suffering from severe over-smoothing. This is achieved by iteratively applying a fixed propagation scheme based on Personalized PageRank, rather than stacking multiple layers that blindly aggregate neighbor information.

However, in APPNP, the teleport probability,  $\alpha$ , enforces a fixed trade-off between local and global information by blending the original node embeddings with the propagated neighbor information at every iteration. This blending is uniformly applied to all nodes, regardless of their structural roles or contextual needs. To address this limitation, a Gated Recurrent Unit (GRU) is incorporated to the APPNP architecture after the  $K$  power iterations to enable a more flexible, per-node and per-feature gating mechanism. The GRU adaptively learns how much information to retain from the original embeddings versus the propagated and blended representations, allowing for node-specific soft mixing. Therefore, instead of embedding the *softmax* function in **Equation (2.3)**, the GRU-enhanced APPNP is calculated as follows:

$$Z^{(K)} = (1 - \alpha)\hat{A}Z^{(K-1)} + \alpha H \quad (2.5)$$

$$R = \sigma(Z^{(K)}W_r + HU_r + b_r) \quad (2.6)$$

$$A = \sigma(Z^{(K)}W_a + HU_a + b_a) \quad (2.7)$$

$$\tilde{H} = \tanh(Z^{(K)}W_h + (R \odot H)U_h + b_h) \quad (2.8)$$

$$Z^{(K)}_{GRU} = (1 - A) \odot H + A \odot \tilde{H} \quad (2.9)$$

where  $W_r, W_a, W_h, U_r, U_a, U_h, b_r, b_a, b_h$ , are learnable parameters.  $\sigma$  is a sigmoid activation function.

In summary, the APPNP structure supports efficient deep information propagation while mitigating over-smoothing. To capture node-level heterogeneity, a GRU is integrated into the APPNP architecture, allowing per-node, per-feature soft blending of local and global information. In the context of LiDAR detection modeling, for a specific target vehicle, the network can efficiently, effectively, and adaptively embed and propagate the features from the AV, intermediate vehicles, to the target vehicle, and predict the TP and FN detection results.

### 3. DATA PREPARATION & MIDAR EVALUATION

This section first introduces the nuScenes AD dataset and the CenterPoint LiDAR detection algorithm, which are used to label the TPs and FNs on the perfect detection results and serve as the training dataset for the MIDAR model. Then, the training and evaluation of MIDAR is elaborated.

#### 3.1 NuScenes Dataset

The nuScenes dataset (19) is a widely used large-scale public dataset for AD. It comprises 1,000 driving scenes collected in Boston and Singapore, two cities that are known for their dense traffic and highly challenging driving situations. The dataset contains a diverse set of traffic scenarios across different locations, weather conditions, vehicle types, and both left- and right-hand traffic, which helps enhance the generalization of MIDAR. **Figure 3** shows an example of the 3D object detection results of one frame in the nuScenes dataset.



Figure 3 3D Object Detection on NuScenes

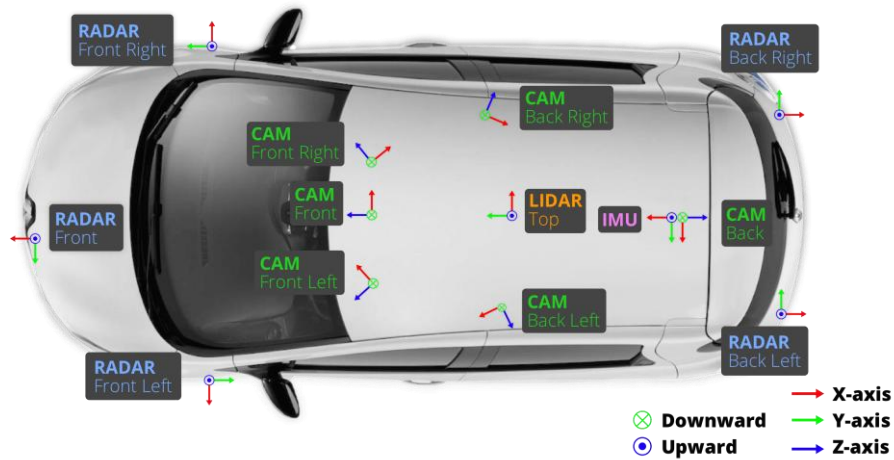


Figure 4 Data-collection Vehicle Setup of NuScenes



**Figure 4** shows the placement of the sensors on the vehicles for data collection in the nuScenes dataset, comprising one spinning LiDAR (Velodyne HDL32E), six cameras (Basler acA1600-60gc), five long-range radar sensors (Continental ARS 408-21) and one IMU & GPS (Advanced Navigation Spatial), among which LiDAR is the only sensing modality used for training MIDAR. Its specifications are detailed below:

- 20Hz capture frequency
- 32 beams, 1080 ( $\pm 10$ ) points per ring
- 32 channels
- 360° horizontal Field of View (FOV),  $+10^\circ$  to  $-30^\circ$  vertical FOV, uniform azimuth angles
- 80m-100m range, usable returns up to 70 meters,  $\pm 2$  cm accuracy
- Up to  $\sim 1.39$  million points per second

### 3.2 CenterPoint LiDAR Detection Algorithm

CenterPoint, a widely adopted and well-established LiDAR-based 3D object detection algorithm, is used to generate the LiDAR detection results from the nuScenes dataset. As illustrated in **Figure 5**, CenterPoint (20) employs a 3D backbone to extract BEV features from LiDAR point clouds, followed by a 2D CNN head to detect object centers and regress 3D bounding boxes. It further refines box predictions using point features extracted at the centers of each box face, passed through an MLP for Intersection-over-Union (IoU)-guided confidence scoring and box refinement.

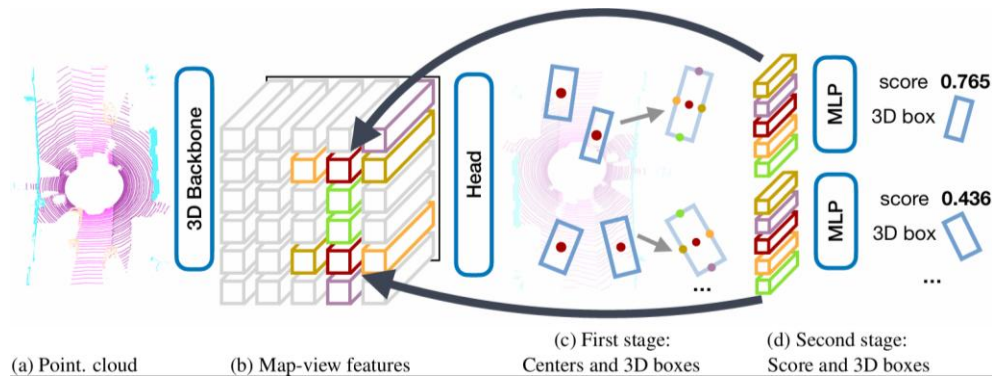


**Figure 5 Overview of CenterPoint (20)**

#### 3.2.1 Training of CenterPoint

The whole nuScenes dataset, comprising 1,000 scenes and 40,000 annotated key frames, is used to train and evaluate the CenterPoint LiDAR detection algorithm. To enrich the sparse LiDAR point clouds, each ground-truth object aggregates information from up to 10 past LiDAR sweeps, captured at 10 Hz. The dataset is split into 70% for training, 15% for validation, and 15% for testing.

We implement CenterPoint with mmdetection3D (24), and train it with the AdamOneCycle (25) optimizer with a learning rate of  $1e-3$  and a weight decay of  $1e-2$ . Focal loss (26) is used for classification, while Smooth L1 loss is used for regression. Only vehicle-related classes are considered, including car, truck, construction vehicle, bus, and trailer. A voxel size of (0.075 m, 0.075 m, 0.2 m) and a point cloud range of (-54 m, -54 m, -5 m) to (54 m, 54 m, 3 m) are adopted. The model is trained for 20 epochs. Data augmentation techniques include ground-truth sampling, random flipping, rotation, scaling, and translation.

#### 3.2.2 Evaluation of CenterPoint

The performance of CenterPoint is evaluated on the testing dataset, with results for vehicle-related classes presented in **Table 1**. The model demonstrates strong detection performance for cars, trucks, and buses, achieving an Average Precision (AP) of 0.85 for cars. In contrast, performance on trailers and construction vehicles is relatively lower, likely due to limited training samples and frequent occlusions. Overall,

CenterPoint provides reliable LiDAR detection results and serves as the target detection model for MIDAR to mimic.

**Table 1 Performance of CenterPoint**

Class	AP	ATE	ASE	AOE	AVE	AAE
Car	0.850	0.179	0.155	0.149	0.206	0.183
Truck	0.567	0.315	0.181	0.139	0.188	0.216
Bus	0.703	0.330	0.185	0.100	0.343	0.263
Trailer	0.382	0.516	0.196	0.595	0.166	0.179
Construction Vehicle	0.181	0.731	0.423	0.899	0.118	0.305

### 3.3 MIDAR Training Dataset Generation

As previously mentioned, MIDAR approximates realistic LiDAR detection by distinguishing TPs and FNs on the ground-truth (GT) bounding boxes, i.e., the entire surrounding vehicles within the LiDAR detection range. To generate the training dataset for MIDAR, we apply the trained CenterPoint model to the testing dataset of nuScenes to generate predicted bounding boxes, which are then used to label either TP (0) or FN (1) on each GT surrounding vehicle. The final labelled data as well as the surrounding vehicles' features are used to train the MIDAR model.

Prior to the labelling, vehicles and objects outside drivable areas are removed from both predictions and ground truth using the nuScenes API and map data, to better reflect traffic simulation environments (or trajectory datasets) and simplify MIDAR's learning task. GT vehicles beyond CenterPoint's detection range are also excluded to ensure spatial alignment between the two sources.

Then, the following steps are taken to label the TP and FN on the GT data, based on the predictions made by CenterPoint:

- (1) For a frame of GT bounding boxes, find the corresponding frame of CenterPoint predictions with the same timestamp.
- (2) Filter the predicted bounding boxes by only considering predictions with detection confidence scores above a predefined threshold (i.e., 0.4).
- (3) Group the GT and predictions by object class, i.e., compare GT and predicted bounding boxes with the same class.
- (4) Compute the 3D IoU between each GT and the predicted bounding box. For each object class, a cost matrix is formed, where each entry represents the negative IoU between a GT and a predicted bounding box.
- (5) Use a Hungarian algorithm (27) to find the optimal set of one-to-one matches between the GT and predicted bounding boxes, by minimizing the cost matrix (i.e., maximizing total IoU).
- (6) Keep the matches between the GT and predicted bounding boxes only if their IoU exceeds a class-specific threshold (e.g., 0.7 for cars, 0.5 for other types of vehicles).
- (7) Finally, GT bounding boxes without valid matches are labeled as FNs, while the matched ones are considered TPs. Remaining unmatched predicted bounding boxes are labeled as FPs.

The median number of TPs, FNs, and FPs across all frames are 6, 4, and 2, respectively, where the number of FNs is about two times that of FPs. The results validate our assumptions that FNs are the primary source of detection errors.

### 3.4 Training and Evaluation of MIDAR

A total of 150 scenes in the nuScenes testing split are used to generate the training dataset for MIDAR. We split the dataset into training and testing subsets using an 80:20 ratio.

MIDAR is trained using the AdamW optimizer (28) with a learning rate of  $1e-4$  and a weight decay of  $1e-5$ . AdamW optimizer is a variant of the Adam optimizer (29) that decouples weight decay from the gradient update, which improves generalization and training stability. The loss function used is cross entropy (30). The model adopts a two-layer MLP to generate the node embeddings, followed by an

approximate Personalized PageRank with six power iterations ( $K = 6$ ) and a teleport probability  $\alpha = 0.1$ . A GRU is integrated into the propagation. The hidden dimension of all layers is set to 128, and a dropout rate of 0.3 is applied for regularization. The model is trained for 70 epochs.

**Table 2** shows MIDAR’s performance with a classification threshold of 0.4. An AUC of 0.909 demonstrates MIDAR’s strong capability in identifying TPs and FNs from perfect LiDAR detection results. Additionally, a classification threshold of 0.4 yields a well-balanced trade-off between precision and recall.

**Table 2 Performance of MIDAR**

	AUC	Precision	Recall	Accuracy	F1
Threshold=0.4	0.909	0.725	0.763	0.840	0.743

## 4. IMPLEMENTATION OF MIDAR

In this section, we first introduce two baseline models that approximate LiDAR detection results, which are widely adopted in current studies. Then two CP-based applications are introduced and their performance under different Lidar detection models are compared.

### 4.1 Baseline LiDAR Detection Models

Two baseline LiDAR detection models, Perfect Detection and Random Dropout, are introduced below.

In Perfect Detection, all surrounding vehicles within the LiDAR detection range are assumed to be perfectly observed. The detection range is a predefined parameter and keeps a constant throughout the entire simulation period or study area. In this paper, this fixed detection range is set to match the point cloud range used in CenterPoint for fair comparison, i.e.,  $(-54 \text{ m}, -54 \text{ m})$  to  $(54 \text{ m}, 54 \text{ m})$ . As most microscopic traffic simulators and trajectory datasets only contain  $x$  and  $y$  dimensions, the height dimension ( $z$ -axis) is not considered. The Perfect Detection model is equivalent to 100% TPs and 0% FNs.

In Random Dropout, vehicles within the LiDAR detection range are randomly dropped (i.e., labeled as FNs). The dropout probability increases with the increase of the distance between the vehicle to the AV. Typically, a set of probabilities for different distance intervals (e.g., for 10% for 0–10 m, 20% for 10–20 m, etc.) are defined. In this paper, the probabilities are aggregated from MIDAR’s precision results. Note that the probabilities are context-dependent and may vary across different simulation platforms, trajectory datasets, and traffic scenarios.

### 4.2 Application 1: CP-based Traffic Signal Control

#### 4.2.1 Application Background

Adaptive traffic signal control (TSC) plays a critical role in managing and optimizing the flow of vehicles at intersections. Traditional approaches rely on fixed-location detectors (e.g., loop detectors), which provide limited spatial coverage and may fail to capture the full dynamics of traffic, thereby reducing control effectiveness. Recent studies (14) have demonstrated that CP-based TSC, which fuses observations from multiple AVs near intersections, can substantially improve the control performance even under very low market penetration rates (MPRs).

#### 4.2.2 Application Setup

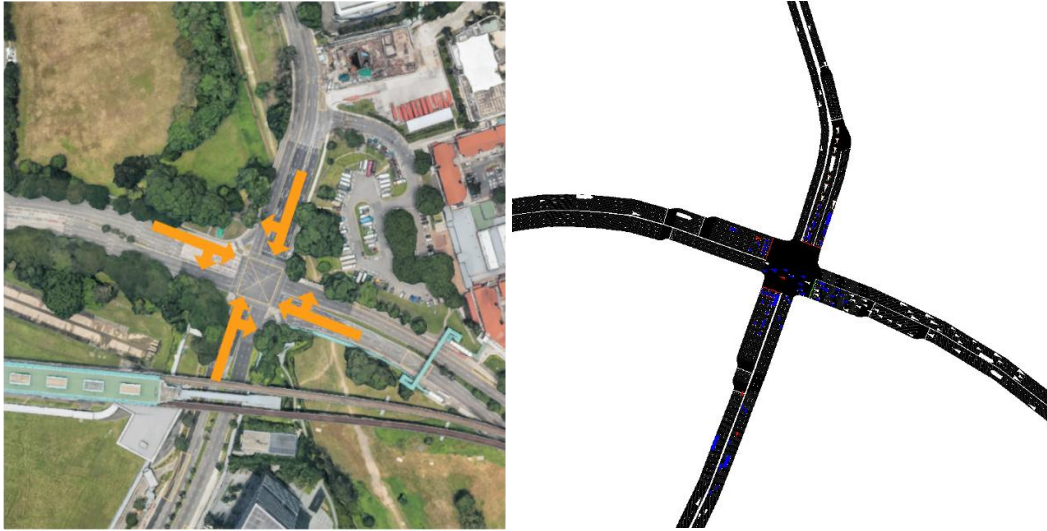
A real-world intersection of Commonwealth Avenue and North Buona Vista Road in Singapore, is selected as the study area to evaluate the performance under different LiDAR detection models, as shown in **Figure 6(a)**. We use SUMO (31), a widely accepted open-source microscopic traffic simulation platform, to conduct the experiments. The SUMO network of the same intersection is shown in **Figure 6(b)**.

The intersection is located exactly where the nuScenes dataset was collected. To further enhance realism, traffic volumes at the intersection are obtained through the Singapore Land Transport Authority’s Data Mall API (32), which collects real-time traffic flow data from loop detectors. Additionally, the vehicle composition in SUMO is configured to match the vehicle class distribution observed in the nuScenes dataset.

A split 4-phase signal timing plan is used, represented by orange arrows in **Figure 6(a)**, same as in real-world operations. Each phase corresponds to movements from the Eastbound, Westbound, Southbound, and Northbound directions, with protected right turns (for left-hand traffic). A 5-s minimum green time and a 40-s maximum green time are adopted. A 4-s yellow and a 1-s all-red clearance interval are enforced between each phase transition. The I-SIG algorithm (33) is selected as adaptive signal control model. The I-SIG algorithm utilizes dynamic programming (DP) to optimize signal phase duration and sequences with the objective of minimizing total delay. To solve the DP problem, an arrival table is constructed and serves as the input, which comprises predictions of future arrival flows for each phase at each timestamp. In this study, the arrival table can be directly constructed using observed vehicle information from the CP environment.

Each simulation run lasts for 3600s with a 0.1s resolution. The first 100 s are considered as the warm-up stage when the signal is controlled by a fixed-time TSC. The vehicle arrival follows a Poisson process generated by SUMO. We set MPR of AVs to 3% which is similar as in (14). The MPR represents the early stage of AV deployment. As shown in **Figure 6(b)**, red vehicles represent AVs, blue vehicles indicate vehicles detected by AVs, and the remaining white vehicles correspond to unobserved vehicles. The I-SIG algorithm constructs the arrival table based on red and blue vehicles' information and optimizes the signal timing.

The Traffic Control Interface (TraCI) in SUMO is used to integrate the LiDAR detection models. For each AV at each time step, one selected LiDAR detection model (Perfect Detection, Random Dropout, or MIDAR) is applied. As mentioned before, the set of dropout probabilities for Random Dropout within different distance intervals are aggregated from MIDAR's precision results: (1) 0-10m: 19.2%; (2) 10-20m: 24.9%; (3) 20-30m: 23.5%; (4) 30-40m: 23.9%; (5) 40-50m: 23.4%; (6) 50-54m: 23.3%. After obtaining the detection results of each AV (i.e., determination of observed and unobserved vehicles), a simple fusion algorithm is applied to remove redundant vehicles and generates a collective CP observation.



(a) A real-world intersection at Commonwealth Ave & N Buona Vista Rd in Singapore

(b) The intersection in SUMO integrated with CP

**Figure 6 Illustrations of a Real-world Intersection and its SUMO Simulation.**

#### 4.2.3 Performance Comparison

We use the average vehicle delay to represent the performance of the signal control model. After running 10 rounds of experiments with different random seeds, **Figure 7** presents the vehicle delay of I-SIG under different LiDAR detection models. The average delay for Perfect Detection, Random Dropout, and MIDAR are 58.12 s, 60.26 s, and 64.09 s, respectively. One-tailed Welch's *t*-tests reveal a statistically significant difference between MIDAR and Perfect Detection ( $p=0.005$ ), and an approaching significant difference

between MIDAR and Random Dropout ( $p=0.063$ ), both at the 5% level. However, such significance is not observed between Perfect Detection and Random Dropout ( $p=0.189$ ). In most cases, MIDAR yields the highest or near-highest delay, indicating that a realistic LiDAR detection model can negatively impact the performance of traffic signal control algorithm, compared with simplified models. However, in Cases 1 and 10, the delay under MIDAR is notably lower than the highest, suggesting that the impact of LiDAR detection patterns is not always consistent. This can be explained by the data requirement of the adaptive traffic signal application. For the I-SIG algorithm, although the arrival table is constructed from individual vehicle information (i.e., speed and distance to stop bar), minimizing the aggregated total delay of each phase is used as the objective function. As a result, as long as the total delay resulted from different LiDAR detection models are similar, the generated traffic signal plans would not deviate too much. In the next application of trajectory reconstruction, we show that different LiDAR detection models have more significant and consistent impact on the performance.

#### 4.2.4 Inference Cost and Runtime Analysis

Running on a desktop featuring an Intel Core i9-13900KF, NVIDIA RTX 4090 GPU, and 64GB DDR5 RAM. The average inference time of MIDAR for a single AV at a single time step is only  $9 \times 10^{-4}$  second, which shows high computational efficiency.

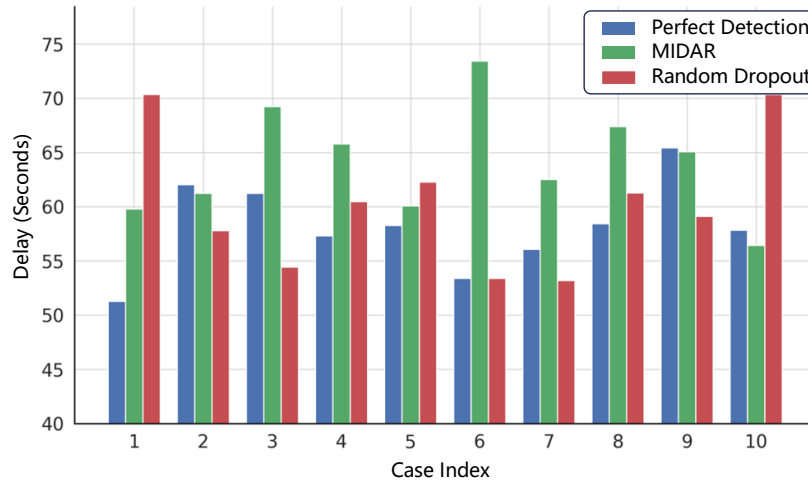


**Figure 7 Performance of I-SIG under Different LiDAR Detection Models**

### 4.3 Application 2: CP-based Vehicle Trajectory Reconstruction

#### 4.3.1 Application Background

Vehicle trajectories are essential for various traffic applications. However, collecting complete vehicle trajectory data using multiple continuously located video cameras or unmanned aerial vehicles, requires high costs. An alternative approach is to reconstruct full trajectories from partial observations, which offers a more cost-effective solution. Existing studies assume that partial observations are collected either in a connected vehicle (CV) environment (34; 35) or in a CP environment (15; 36). For studies that consider CP environment, usually the Perfect Detection model is applied. One exception is the work from Zhang and Feng (15), in which the impact of occlusion is modeled: if a vehicle is entirely in the shadows of other vehicles, it is considered unobservable. However, this is still a simplified model that does not reflect real LiDAR detection patterns.

#### 4.3.2 Trajectory Dataset Preprocessing

Different from the first application that integrates MIDAR into microscopic simulation, in this application, the Next Generation SIMulation (NGSIM) dataset (37) is used to demonstrate the impact of different

LiDAR detection models. The US101 Highway vehicle trajectory dataset is utilized as the study area. The dataset was collected in Los Angeles, California, during the morning peak period (7:50 a.m. - 8:05 a.m.). Our analysis focuses on a 500-meter stretch of the highway encompassing all six lanes. The study area is delineated by infrastructure sensors, as illustrated in **Figure 8**, which defines the start and end of the study area. The infrastructure sensors provide the initial and final states of vehicles, which are necessary to the trajectory reconstruction model.

An optimization-based model from Zhu et al. (38) is employed to reconstruct vehicle trajectories. The model effectively captures lane-change and overtaking behaviors and functions under very low AV market penetration rates (MPRs) with CP. Specifically, the reconstruction task is formulated as a mixed integer linear programming (MILP) problem with the objective of minimizing the errors between reconstructed and observed AV trajectories, which converts the trajectory reconstruction problem into a joint trajectory generation problem. The model incorporates various constraints on decision variables, vehicle dynamics, lane-changing behavior, and safety to ensure realistic and feasible outputs. When implemented, the model simultaneously generates the longitudinal position and lane index of each vehicle at each time step.

The original US101 dataset is pre-processed to generate the CP data under an MPR of 3% of AVs, which are uniformly sampled in the trajectory dataset within the 15 minutes time period. A total of 59 AVs is sampled, which report their own trajectories and detected trajectories of its surrounding vehicles. Since the NGSIM data contain ground truth of all vehicle trajectories, the three LiDAR detection models can be easily applied, similar as in the first application. The probabilities of Random Dropout are as follows: (1) 0-10m: 2.6%; (2) 10-20m: 1.7%; (3) 20-30m: 7.1%; (4) 30-40m: 23.1%; (5) 40-50m: 41.9%; (6) 50-54m: 48.6%. Note that a common limitation of most trajectory datasets including NGSIM is the absence of vehicle height information, which is essential for MIDAR. To overcome this, a linear regression model is trained on the nuScenes dataset to estimate vehicle height based on vehicle length and width. The regressed model is then applied to the US101 dataset to infer height information.

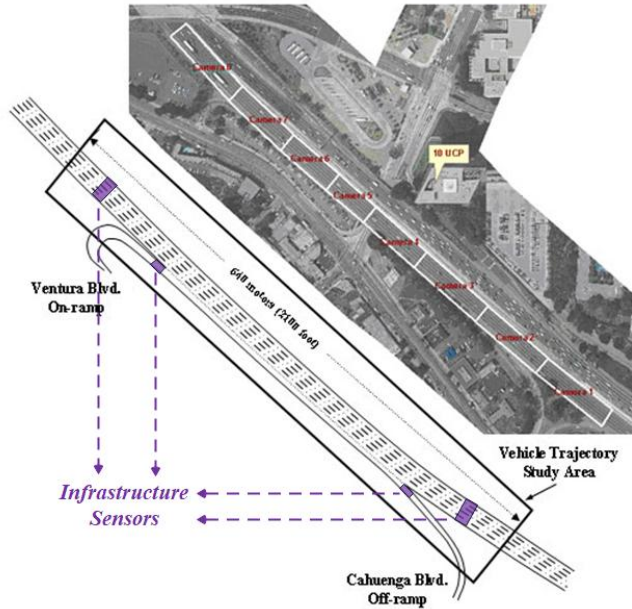


**Figure 8** Study Area on US101 Highway

#### 4.3.3 Performance Comparison

**Figure 9** compares the performance of the vehicle trajectory reconstruction Mean Absolute Errors (MAEs) over all 58 scenarios under the three LiDAR detection models. The average MAEs for Perfect Detection, Random Dropout, and MIDAR are 1.84 m, 2.06 m, and 2.56 m, respectively. MIDAR consistently produces



the highest MAE across nearly all planning horizons. Welch's  $t$ -tests are also conducted and reveal the same trend: a statistically significant difference is found between MIDAR and Perfect Detection ( $p=0.001$ ), as well as between MIDAR and Random Dropout ( $p=0.017$ ). In contrast, no significant difference is observed between Perfect Detection and Random Dropout ( $p=0.160$ ). These results indicate that the trajectory reconstruction application requires more accurate and disaggregated individual vehicle information such as location, speed, and lane index, so that the impact of different LiDAR detection patterns is more stable and significant. Notably, even in Random Dropout, despite sharing the same aggregated detection precision level (i.e., the proportion of trajectory points to be constructed are similar as in MIDAR), fails to replicate the characteristics of LiDAR detection patterns and significantly affects the performance. This finding highlights the necessity of employing MIDAR, which captures more accurately real-world data patterns generated from LiDAR detection.



**Figure 9 Performance of the Trajectory Reconstruction Application under Different LiDAR Detection Models**

## 5. CONCLUSIONS

This study presented MIDAR, a LiDAR detection mimicking model designed to approximate realistic LiDAR detection results. An RM-LoS graph was constructed to better capture the impact of surrounding vehicles' layout and dimensions on the detection results. Based on the constructed RM-LoS graph, MIDAR employed a GRU-enhanced APPNP architecture, enabling efficient and adaptive propagation of features from the ego AV to surrounding vehicles. The training dataset for MIDAR was created using the CenterPoint model on the nuScenes AD dataset. With an AUC of 0.909, MIDAR demonstrated strong capability in distinguishing TPs and FNs from complete detection results. To validate the necessity of realistic LiDAR detection modelling, two CP-based traffic applications, adaptive TSC and vehicle trajectory reconstruction, are selected to compare the impact of MIDAR with other two baseline detection models. Performance metrics from both applications highlight the importance of realistic LiDAR detection modeling, particularly for applications require accurate vehicle-level information.

The main limitation of this study lies in simplifying LiDAR detection outcomes to only TPs and FNs, while ignoring FPs. Although challenging, future research could explore how to model FPs, for example, by introducing candidate nodes into the graph based on empirical experience to represent potential FPs.

## ACKNOWLEDGMENTS

This research is supported in part by the U.S. National Science Foundation (NSF) through Grant CPS 2038215, and U.S. Department of Transportation (USDOT) Region 5 University Transportation Center (Center for Connected and Automated Transportation). The views presented in this paper are those of the authors alone.

## AUTHOR CONTRIBUTIONS

The authors confirm their contribution to the paper as follows: study conception and design: Zhu, and Feng; data collection: Zhu; analysis and interpretation of results: Zhu; draft manuscript preparation: Zhu, and Feng. All authors reviewed the results and approved the final version of the manuscript.

## REFERENCES

- [1] The Robot Report. *Waymo reaches 100M fully autonomous miles across all deployments*. <https://www.therobotreport.com/waymo-reaches-100m-fully-autonomous-miles-across-all-deployments/>.
- [2] Ye, L., and T. Yamamoto. Evaluating the impact of connected and autonomous vehicles on traffic safety. *Physica A: Statistical Mechanics and its Applications*, Vol. 526, 2019, p. 121009.
- [3] Garg, M., and M. Bouroche. Can connected autonomous vehicles improve mixed traffic safety without compromising efficiency in realistic scenarios? *IEEE Transactions on Intelligent Transportation Systems*, Vol. 24, No. 6, 2023, pp. 6674-6689.
- [4] Peng, B., M. F. Keskin, B. Kulcsár, and H. Wymeersch. Connected autonomous vehicles for improving mixed traffic efficiency in unsignalized intersections with deep reinforcement learning. *Communications in Transportation Research*, Vol. 1, 2021, p. 100017.
- [5] Luo, L., Y. Liu, Y. Feng, H. X. Liu, and Y.-E. Ge. Stabilizing traffic flow by autonomous vehicles: Stability analysis and implementation considerations. *Transportation Research Part C: Emerging Technologies*, Vol. 158, 2024, p. 104449.
- [6] Wang, S., M. Shang, M. W. Levin, and R. Stern. A general approach to smoothing nonlinear mixed traffic via control of autonomous vehicles. *Transportation Research Part C: Emerging Technologies*, Vol. 146, 2023, p. 103967.
- [7] Chen, B., Y. Chen, Y. Wu, Y. Xiu, X. Fu, and K. Zhang. The effects of autonomous vehicles on traffic efficiency and energy consumption. *Systems*, Vol. 11, No. 7, 2023, p. 347.
- [8] Malik, S., and W. Sun. Analysis and simulation of cyber attacks against connected and autonomous vehicles. In *2020 International Conference on Connected and Autonomous Driving*, IEEE, 2020. pp. 62-70.



- [9] Dosovitskiy, A., G. Ros, F. Codevilla, A. Lopez, and V. Koltun. CARLA: An open urban driving simulator. In *Conference on Robot Learning*, PMLR, 2017. pp. 1-16.
- [10] Rong, G., B. H. Shin, H. Tabatabaee, Q. Lu, S. Lemke, M. Možeiko, E. Boise, G. Uhm, M. Gerow, and S. Mehta. Lgsvl simulator: A high fidelity simulator for autonomous driving. In *2020 IEEE 23rd International Conference on Intelligent Transportation Systems*, IEEE, 2020. pp. 1-6.
- [11] Shah, S., D. Dey, C. Lovett, and A. Kapoor. Airsim: High-fidelity visual and physical simulation for autonomous vehicles. In *Field and Service Robotics: Results of the 11th International Conference*, Springer, 2017. pp. 621-635.
- [12] Bai, Z., G. Wu, M. J. Barth, Y. Liu, E. A. Sisbot, K. Oguchi, and Z. Huang. A survey and framework of cooperative perception: From heterogeneous singleton to hierarchical cooperation. *IEEE Transactions on Intelligent Transportation Systems*, 2024.
- [13] Fang, S., J. Liu, M. Ding, Y. Cui, C. Lv, P. Hang, and J. Sun. Towards interactive and learnable cooperative driving automation: a large language model-driven decision-making framework. *IEEE Transactions on Vehicular Technology*, 2025.
- [14] Li, W., T. Zhu, and Y. Feng. A cooperative perception based adaptive signal control under early deployment of connected and automated vehicles. *Transportation Research Part C: Emerging Technologies*, Vol. 169, 2024, p. 104860.
- [15] Zhang, C., and Y. Feng. Vehicle trajectory reconstruction for freeway traffic considering lane changing behaviors. *Journal of Intelligent Transportation Systems*, 2024, pp. 1-16.
- [16] Zhang, K., and Y. M. Nie. Mitigating the impact of selfish routing: An optimal-ratio control scheme (ORCS) inspired by autonomous driving. *Transportation Research Part C: Emerging Technologies*, Vol. 87, 2018, pp. 75-90.
- [17] Guo, Q., X. J. Ban, and H. A. Aziz. Mixed traffic flow of human driven vehicles and automated vehicles on dynamic transportation networks. *Transportation Research Part C: Emerging Technologies*, Vol. 128, 2021, p. 103159.
- [18] Li, T., X. Han, and J. Ma. Cooperative perception for estimating and predicting microscopic traffic states to manage connected and automated traffic. *IEEE Transactions on Intelligent Transportation Systems*, Vol. 23, No. 8, 2021, pp. 13694-13707.
- [19] Caesar, H., V. Bankiti, A. H. Lang, S. Vora, V. E. Liong, Q. Xu, A. Krishnan, Y. Pan, G. Baldan, and O. Beijbom. nuscenes: A multimodal dataset for autonomous driving. In *Proceedings of the IEEE/CVF Conference on Computer Vision and Pattern Recognition*, 2020. pp. 11621-11631.
- [20] Yin, T., X. Zhou, and P. Krahenbuhl. Center-based 3d object detection and tracking. In *Proceedings of the IEEE/CVF Conference on Computer Vision and Pattern Recognition*, 2021. pp. 11784-11793.
- [21] Yu, M. Y., R. Vasudevan, and M. Johnson-Roberson. Occlusion-Aware Risk Assessment for Autonomous Driving in Urban Environments. *IEEE Robotics and Automation Letters*, Vol. 4, No. 2, 2019, pp. 2235-2241.
- [22] Garey, M., D. Johnson, and H. So. An application of graph coloring to printed circuit testing. *IEEE Transactions on Circuits and Systems*, Vol. 23, No. 10, 1976, pp. 591-599.
- [23] Gasteiger, J., A. Bojchevski, and S. Günnemann. Predict then propagate: Graph neural networks meet personalized pagerank. *arXiv preprint arXiv:1810.05997*, 2018.
- [24] MMDetection3D Contributors. *OpenMMLab's Next-generation Platform for General 3D Object Detection*. <https://github.com/open-mmlab/mmdetection3d>.
- [25] Smith, L. N. A disciplined approach to neural network hyper-parameters: Part 1--learning rate, batch size, momentum, and weight decay. *arXiv preprint arXiv:1803.09820*, 2018.
- [26] Lin, T.-Y., P. Goyal, R. Girshick, K. He, and P. Dollár. Focal loss for dense object detection. In *Proceedings of the IEEE International Conference on Computer Vision*, 2017. pp. 2980-2988.
- [27] Kuhn, H. W. The Hungarian method for the assignment problem. *Naval Research Logistics Quarterly*, Vol. 2, No. 1-2, 1955, pp. 83-97.
- [28] Loshchilov, I., and F. Hutter. Decoupled weight decay regularization. *arXiv preprint arXiv:1711.05101*, 2017.

- [29] Kingma, D. P., and J. Ba. Adam: A method for stochastic optimization. *arXiv preprint arXiv:1412.6980*, 2014.
- [30] Goodfellow, I., Y. Bengio, A. Courville, and Y. Bengio. *Deep learning*. MIT press Cambridge, 2016.
- [31] Lopez, P. A., M. Behrisch, L. Bieker-Walz, J. Erdmann, Y.-P. Flötteröd, R. Hilbrich, L. Lücken, J. Rummel, P. Wagner, and E. Wießner. Microscopic traffic simulation using sumo. In *2018 21st International Conference on Intelligent Transportation Systems*, IEEE, 2018. pp. 2575-2582.
- [32] Land Transport Authority. *Data Mall API*. <https://datamall.lta.gov.sg>.
- [33] Feng, Y., K. L. Head, S. Khoshmashgham, and M. Zamanipour. A real-time adaptive signal control in a connected vehicle environment. *Transportation Research Part C: Emerging Technologies*, Vol. 55, 2015, pp. 460-473.
- [34] Chen, P., L. Wei, F. Meng, and N. Zheng. Vehicle trajectory reconstruction for signalized intersections: A hybrid approach integrating Kalman Filtering and variational theory. *Transportmetrica B: Transport Dynamics*, Vol. 9, No. 1, 2020, pp. 22-41.
- [35] Wei, L., Y. Wang, and P. Chen. A Particle Filter-Based Approach for Vehicle Trajectory Reconstruction Using Sparse Probe Data. *IEEE Transactions on Intelligent Transportation Systems*, Vol. 22, No. 5, 2021, pp. 2878-2890.
- [36] Chen, X., G. Qin, T. Seo, J. Yin, Y. Tian, and J. Sun. A macro-micro approach to reconstructing vehicle trajectories on multi-lane freeways with lane changing. *Transportation Research Part C: Emerging Technologies*, Vol. 160, 2024, p. 104534.
- [37] NGSIM. *The Next Generation Simulation Program*. <https://ops.fhwa.dot.gov/trafficanalysisistools/ngsim.htm>.
- [38] Zhu, T., W. Li, and Y. Feng. Integrated Optimization for Vehicle Trajectory Reconstruction under Cooperative Perception Environment. *Transportation Research Part C: Emerging Technologies*, In Revision.